Microwave signatures of the $\mathbb{Z}_2$ and $\mathbb{Z}_4$ fractional Josephson effects

P. L. S. Lopes, S. Boutin, P. Karan, U. C. Mendes, and I. Garate
Institut Quantique and Département de Physique, Université de Sherbrooke, Sherbrooke, Québec, Canada J1K 2R1

(Received 5 October 2018; published 2 January 2019)

We present a many-body exact diagonalization study of the $\mathbb{Z}_2$ and $\mathbb{Z}_4$ Josephson effects in circuit quantum electrodynamics architectures. Numerical simulations are conducted on Kitaev chain Josephson junctions hosting nearest-neighbor Coulomb interactions. The low-energy effective theory of highly transparent Kitaev chain junctions is shown to be identical to that of junctions created at the edge of a quantum spin Hall insulator. By capacitively coupling the interacting junction to a microwave resonator, we predict signatures of the fractional Josephson effects on the cavity frequency and on time-resolved reflectivity measurements.

DOI: 10.1103/PhysRevB.99.045103

I. INTRODUCTION

Josephson junctions (JJs) built at the edges of quantum spin Hall (QSH) insulators have been predicted to display a rich variety of phenomena, which emerge from the interplay between time-reversal (TR) symmetry and the conservation of a local fermion parity. In the presence of a dc voltage bias, three theoretical scenarios have been proposed, with distinct periodicities of the Josephson current on the superconducting phase difference across the junction [1–5].

In the first scenario, concerning noninteracting and TR-symmetric JJs, an ac 2π-periodic Josephson effect takes place, together with a dissipative dc current [1,2]. This is the ordinary Josephson effect for perfectly transparent weak links. In the second scenario, involving JJs with broken TR symmetry, the current is dissipationless and its period doubles to 4π. Such doubling is the hallmark of hybridized Majorana zero modes (MZMs) at the edges of the weak link [3]. In the third scenario, entailing TR-symmetric JJs with short-range interactions, the current is nondissipative and 8π periodic [4,5]. This effect has been attributed to TR-protected $\mathbb{Z}_4$ parafermions, fractionalized quasiparticles of conceptual and practical interest [4]. The 4π-periodic ($\mathbb{Z}_2$) and 8π-periodic ($\mathbb{Z}_4$) Josephson effects are known as "fractional," as opposed to the "integer" 2π-periodic Josephson effect.

The experimental realization of fractional Josephson effects constitutes an active research topic in topological condensed matter physics. Unexpectedly, recent experiments on QSH JJs have reported Shapiro steps and Josephson radiation consistent with a 4π-periodic Josephson effect [6–9] instead of the 2π-periodic or 8π-periodic effects that would have been anticipated for such a TR-symmetric system. Consistent explanations for this phenomenon have been put forward in terms of exchange interactions between QSH edge states and nearby charge puddles, which can act as magnetic impurities [10] as well as in terms of two-particle inelastic scattering [11].

The 8π Josephson effect remains experimentally elusive to this day. Its observation requires weak links of lengths comparable to, or larger than, the superconducting (SC) coherence length. In addition, a many-body energy gap produced by TR-preserving interactions is needed. For umklapp interactions, such a gap develops only in the strong-coupling limit [4,5]. To date, it is unclear whether the condition of strong interactions may be satisfied in real QSH JJs. In contrast, spin-flip interactions with magnetic impurities can generate 8π periodicity both at strong and weak coupling [2,10,12]. Nevertheless, in the weak-coupling regime, interactions with magnetic impurities give a dominant 4π periodicity [10]. In addition, for magnetic impurities of spin higher than $\frac{1}{2}$, particularities of the single-ion anisotropies can give rise to 2π and 4π periodicities.

In view of the aforementioned challenges, it would be of interest to (i) identify alternative systems where the 8π-periodic Josephson effect can occur, and (ii) develop alternative ways to measure it. The main objective of this work is to make theoretical progress along these lines. Concerning (i), we establish that the 8π-periodic Josephson effect can take place in JJs built out of Kitaev chains [13], i.e., one-dimensional lattices of spinless fermions with p-wave superconductivity. The proposals for physical realizations of Kitaev chains are numerous and under intense experimental investigation (see [14] and references therein). Concerning (ii), we propose signatures of the 8π Josephson effect in circuit quantum electrodynamics (cQED) architectures.

Our study begins in Sec. II, where we show that a Kitaev chain JJ has the same low-energy effective field theory as the QSH JJ. This equivalence holds provided that the lattice model is tuned to the regime of a perfectly transparent junction (Sec. II A). In this regime, the lattice model is endowed with an effective low-energy TR symmetry operator squaring to -1, which mimics that of the QSH JJ. Because the low-energy states of the junction are localized within the weak link, finite-sized superconducting electrodes suffice to achieve a good agreement between the continuum and lattice theories (Secs. II B and II C). Therefore, we can access physical observables of strongly interacting QSH JJs via exact diagonalization of the Kitaev chain JJ. Specifically, we carry out a lattice analysis of the $\mathbb{Z}_2$ and $\mathbb{Z}_4$ Josephson effects (Secs. II D, II E, and II F). Here, the main advantage over the recent studies of fractional Josephson effects based on bosonization and perturbation theory [2,4,10,12,15] is that we have access to the many-body energies *and* wave functions,

which then allow us to compute physical observables for an arbitrary interaction strength.

In Sec. III, we apply our theory to determine the influence of strong interactions and quasiparticle fractionalization in cQED measurements of topological JJs. Recently, cQED architectures [16] have been explored, both theoretically and experimentally, as promising venues to probe and characterize topological superconductivity in JJs [17–23]. In cQED, a microwave cavity is utilized to monitor, in an efficient and noninvasive way, the discrete energy level dynamics of quantum circuits [23]. Thus far, all cQED studies of topological junctions have neglected the effect of short-range electron-electron interactions. Accordingly, little is known about the cQED signatures of the 8π-periodic Josephson effect. By investigating the response of a microwave resonator coupled to a topological JJ (Sec. III A), we find that the cavity frequency inherits the anomalous Josephson periodicities and displays a series of kinks and peaks (Sec. III B) that can be resolved in the phase shift of the reflected signal (Sec. III D). In contrast, the cavity linewidth is unaffected by the presence of the junction, as long as (i) the broadening of the electronic states is small compared to the cavity frequency, and (ii) the cavity frequency is smaller than the energy gaps that protect the fractional Josephson effects (Sec. III C). Finally, Sec. IV presents the conclusions, and the Appendices contain extra details on the calculations.

II. FRACTIONAL JOSEPHSON EFFECTS IN KITAEV CHAIN JUNCTIONS

The objective of this section is to establish an equivalence between the Kitaev chain JJ and the QSH JJ at low energies. We begin by demonstrating that the low-energy continuum expansion of the lattice model exhibits an effective TR symmetry which allows mapping to the QSH JJ. Then, we proceed with a pedagogical discussion of the fractional Josephson effects that arise when the effective TR symmetry is broken or many-body interactions are turned on. After that, many-body spectra and wave functions for the 4π- and 8π-periodic scenarios are obtained by exact diagonalization of the lattice model. One important conclusion from this section is that the 8π Josephson effect can occur in Kitaev chains. This statement complements that of Ref. [15], where the authors considered an interacting Rashba nanowire with "true" TR symmetry (i.e., no magnetic fields). Here, we demonstrate that the 8π-periodic Josephson effect is also possible in Rashba nanowires placed under magnetic fields because of an effective TR symmetry that emerges at low energies when the JJ has a high transparency.

A. Lattice and continuum models

Figure 1(a) illustrates a Kitaev chain of N sites, whose Hamiltonian reads as

$$H_{\rm JJ} = -\sum_l [(t c_l^\dagger c_{l+1} + \Delta_l c_l c_{l+1} + \text{H.c.}) + \mu c_l^\dagger c_l]. \quad (1)$$

Here, c_l's are fermion operators at site $l \in \{-N/2, \ldots, N/2-1\}$, μ is a uniform chemical potential, $t > 0$ is the hopping parameter, and Δ_l is the complex pairing potential at site l. To obtain a Josephson junction with a weak link of length $N_L - 1$, we consider

$$\Delta_l = \begin{cases} \Delta_0, & l < -N_L/2 \\ 0, & -N_L/2 \leqslant l < N_L/2 \\ \Delta_0 e^{i\varphi}, & l \geqslant N_L/2 \end{cases} \quad (2)$$

where φ is the superconducting phase difference across the junction, and Δ_0 is taken to be real. For simplicity, we take N and N_L to be even. In this spinless model, the TR operation is simply the complex conjugation K. For the JJs studied in this work, the charging energy is assumed to be much smaller than the Josephson energy and thus φ is regarded as a c number.

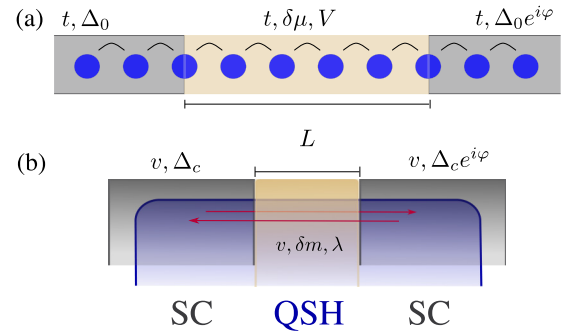

FIG. 1. (a) Cartoon of a Kitaev chain Josephson junction containing N sites (blue). A pair of p-wave superconducting regions (gray) of pairing strength Δ_0 are separated by a normal weak link (yellow) containing N_L sites. The superconducting phase difference is φ. When the hopping amplitude t and the onsite potential for the spinless fermions are uniform throughout the system, an effective TR symmetry squaring to -1 emerges at low energies. Local onsite potentials ($\delta\mu$) break this symmetry, whereas first-neighbor extended Hubbard interactions (V) do not. (b) Cartoon of a quantum spin-Hall Josephson junction, with a pair of helical edge modes (red arrows) of velocity v. At low energies, the Kitaev chain JJ can emulate a QSH JJ. Local onsite potentials and first-neighbor repulsive interactions of the Kitaev JJ map onto magnetic perturbations (δm) and TR-preserving interactions (λ) in QSH JJs, respectively.

Assuming that the chemical potential is well within the bandwidth ($|\mu| \ll 2t$), namely, that the chain is well within the topologically nontrivial phase, we can make a low-energy expansion of the fermionic lattice modes close to the two normal-phase Fermi points: $a^{-1/2} c_l \approx [e^{ik_F x}\psi_R + e^{-ik_F x}\psi_L]$, where a is the lattice constant ($x = la$), $\hbar = 1$, and $\psi_{R,L}$ are slowly fluctuating right- and left-mover fields. The Fermi wave vector k_F is defined through $\mu = -2t\cos k_F a$. To leading order in a gradient expansion of a, and neglecting fast oscillating terms, Eq. (1) becomes

$$H_{\rm JJ}(\varphi) \approx v \int dx (\psi_R^\dagger(-i\partial_x)\psi_R - \psi_L^\dagger(-i\partial_x)\psi_L) + \int dx (\Delta_c \Theta(|x| - L/2) e^{i\Theta(x)\varphi}\psi_L\psi_R + \text{H.c.}), \quad (3)$$

where $\Theta(x)$ is the step function, $v = 2at\sin(k_F a)$ is a velocity, $\Delta_c = 2\Delta_0 \sin(k_F a)$ is the effective pairing potential, $L = (N_L - 1)a$ is the length of the weak link, and the superconducting phase was globally shifted by $\pi/2$. As illustrated

in Fig. 1(b), the same Hamiltonian describes a JJ at the edge of a spin-momentum-locked QSH insulator with proximitized s-wave superconductivity [3,4]. Next, we consider possible antiunitary TR operators, which commute with our low-energy description of $H_{\rm JJ}(\varphi)$.

The lattice level TR operator $\mathcal{T}_+$ acts on the continuum basis by exchanging L and R modes up to a gauge-dependent phase. For Eq. (3), TR acts on the operators as $\mathcal{T}_+\psi_L\mathcal{T}_+^{-1} = i\psi_R$, $\mathcal{T}_+\psi_R\mathcal{T}_+^{-1} = i\psi_L$, and the lattice level symmetry is preserved such that $[H_{JJ}(n\pi), \mathcal{T}_+] = 0$, for $n \in \mathbb{Z}$. Defining a spinor (ψ_R, ψ_L) with the left- and right-moving modes, and a set of Pauli matrices τ_i $(i = x, y, z)$ acting on this space, the so-called *first-quantized* description of this TR operator is $T_+ = i\tau_x K$, with $T_+^2 = +1$. In addition, we can define a second antiunitary operator $\mathcal{T}_-$ which also commutes with Eq. (3) at $\varphi = n\pi$ $(n \in \mathbb{Z})$ and with first-quantized representation $T_- = i\tau_y K$. Since $T_-^2 = -1$, this additional symmetry enforces Kramers degeneracies at TR-invariant superconducting phase differences.

Even though the fermions ψ_R and ψ_L carry no spin degrees of freedom, their Hamiltonian displays the same symmetries and behavior as that of a QSH edge state. Unlike in the case of the QSH edge, however, this $T_- = i\tau_y K$ TR symmetry is only effective. First, it crucially relies on the validity of neglecting the fast oscillating terms in the low-energy expansion leading to Eq. (3). In order to be valid, this approximation requires the superconducting coherence length $\xi_0 = \hbar v/\Delta_c = ta/\Delta_0$ to obey $\xi_0 \gg 2\pi/k_F$, which will be satisfied for lattice parameters such that $t \gg \Delta_0$ $(\xi_0 \gg a)$. Second, certain perturbations of the lattice Hamiltonian (1), such as local spatial inhomogeneities in the hopping parameter or in the chemical potential, produce terms in the continuum approximation that do not commute with $\mathcal{T}_-$, leading to single-body backscattering terms between left and right movers. In short, $\mathcal{T}_-$ is a low-energy symmetry of the Kitaev chain JJ only when the transparency of the junction is unity. Extended Hubbard interactions, the simplest two-body terms in the Kitaev chain, preserve $\mathcal{T}_-$ at low energies. For now, we proceed with the noninteracting and fine-tuned TR-preserving scenario.

B. Single-particle states

In this section, we validate the continuum expansion of the lattice model by calculating and comparing the spectra of Eqs. (1) and (3). This exercise will set the notation for the following sections. Since Eq. (3) has been previously solved [2–4,24], here we review the main results rapidly but pause on some intricacies that are rarely discussed in the literature.

Measuring energies and lengths in units of Δ_c and ξ_0, respectively, Eq. (3) can be recast in the Bogoliubov–de Gennes (BdG) form

$$H_{\rm JJ}(\varphi) \approx \frac{1}{2}\int dx\, \Psi^\dagger h(\varphi)\Psi, \tag{4}$$

where $\Psi = (\psi_R, \psi_L, \psi_L^\dagger, -\psi_R^\dagger)^T$. In this basis, the single-particle BdG Hamiltonian reads as

$$h(\varphi) = [-i\tau_z\partial_x]\rho_z + \Theta(|x| - L/2)\rho_x e^{i\rho_z\Theta(x)\varphi}, \tag{5}$$

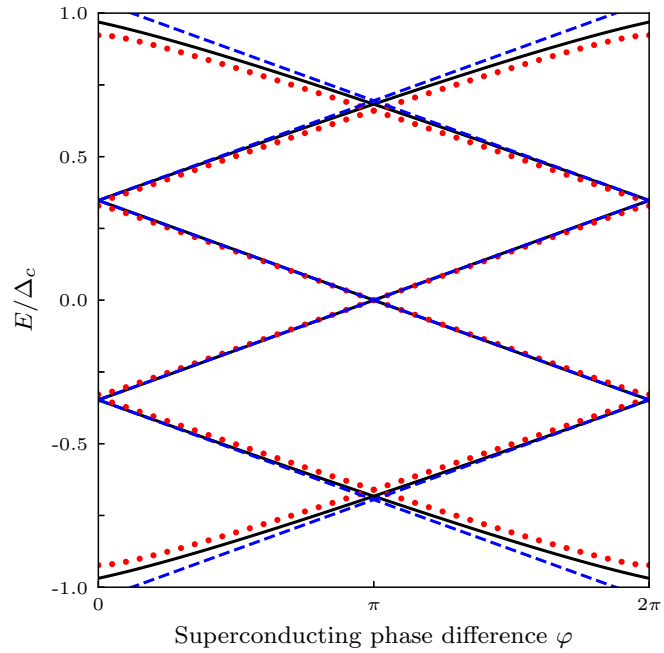

FIG. 2. Noninteracting QSH JJ single-particle spectrum obtained for $\mu = 0$, $\Delta_0 = t/2$ $(\xi_0 = 2a)$. Red dots are obtained from numerical diagonalization of the Kitaev chain JJ ($N_L = 8$, $N = 200$), black full curves are obtained from solving the continuum effective theory [cf. Eq. (7), with $L = 3.5\xi_0$]. No adjustments of parameters are made. Blue dashed curves are obtained by an effective model where the superconducting banks of the junction are substituted by pointlike leads and an effective pairing $\Delta_{\rm eff} \approx 0.77\Delta_0$.

where $L/\xi_0 \to L$, Pauli matrices ρ_i act in the Nambu particle-hole space, and, as mentioned above, τ_i matrices act in the ψ_L, ψ_R space.

Using $[h, \tau_z] = 0$, we decompose the Hilbert space in two τ_z eigensectors and solve

$$h_\tau(\varphi)\psi_\tau = E_\tau\psi_\tau \tag{6}$$

with wave functions of the form $\psi_+ = (u_+, 0, v_+, 0)^T$ and $\psi_- = (0, u_-, 0, v_-)^T$ obeying continuous boundary conditions at $x = \pm L/2$.

1. *Energy spectrum of Eq. (6)*

Let us concentrate on the Andreev bound state (ABS) spectrum, i.e., states with discrete energies inside the bulk SC gap ($|E_\tau| < 1$). The ABS energies are determined by the solutions of the transcendental equation

$$\tan(\tau L E_\tau) = \frac{\sqrt{1 - E_\tau^2} - \tau E_\tau \tan\left(\frac{\varphi}{2}\right)}{\tau E_\tau + \sqrt{1 - E_\tau^2}\tan\left(\frac{\varphi}{2}\right)}, \tag{7}$$

which reduces to an earlier result [4] at $\varphi = \pi$. For each value of φ, the solutions $E_{n,\tau}(\varphi)$ are discrete and labeled with the indices n and τ. The latter index characterizes the slope of the energy eigenvalue as a function of φ: $\tau = +1$ for negative slope, $\tau = -1$ for positive slope.

Figure 2 displays the solutions of Eq. (7) (full black) and a single-particle diagonalization of Eq. (1) (red dots). A good agreement is obtained between the two sets of curves for energies well inside the bulk SC gap. The agreement can be

made even better by increasing the ratio ξ_0/a, which further suppresses the $\mathcal{T}_-$-breaking fast oscillating terms.

The structure of the energy eigenvalues in Fig. 2 is constrained by the Nambu particle-hole operator $C = \rho_y\tau_y K$ and the TR operator $T_- = i\tau_y K$, which impose

$$\begin{aligned}\tau_y\rho_y h(\varphi)\rho_y\tau_y &= -h^*(\varphi),\\ \tau_y h(\varphi)\tau_y &= h^*(-\varphi).\end{aligned} \tag{8}$$

These relations in turn enforce

$$\begin{aligned}E_\tau(\varphi) &= -E_{-\tau}(\varphi),\\ E_\tau(\varphi) &= E_{-\tau}(-\varphi),\end{aligned} \tag{9}$$

where the left- and right-hand sides need not correspond to the same value of n. As a consequence of TR symmetry and the 2π periodicity of the Hamiltonian, different ABS cross at $\varphi = \pi$ (or multiples thereof). The index n can be used to identify these crossings, with $n > 0$ if the crossing happens at positive energies, $n = 0$ if the crossing is at vanishing energy, $n < 0$ for crossings at negative energies. The number M of positive-energy ABS crossings at $\varphi = \pi$ depends on the length of the weak link and is fixed by $-\frac{\pi}{2} < L - M\pi \leqslant \frac{\pi}{2}$, as can be concluded from Eq. (7). With the parameter values of Fig. 2 we have $M = 1$, which is the minimum necessary for the $\mathbb{Z}_4$ Josephson effect to be discussed below. For concreteness, we will keep this number of crossings for the remainder of this paper.

To gain some analytical insight on the characteristic energy scale of the ABS modes, we take an approach of replacing the SC electrodes by pointlike SC leads. In this case, following the standard procedure of effective field theories, we fit for an effective SC pairing strength that returns the correct energy spectrum (see Ref. [25] for an illuminating discussion). After putting back the units, this exercise results in [24]

$$E_{n,\tau} = \frac{\Delta_{\text{eff}}\xi_0}{2L}[\pi(2n+\tau) - \tau\varphi], \tag{10}$$

thereby uncovering the scaling of ABS energies with the Thouless energy $E_T = \Delta_c\xi_0/L = v/L$. Fitting an effective SC pairing of $\Delta_{\text{eff}} \approx 0.77\Delta_c$, one recovers the blue dashed curves in Fig. 2, which again match the numerical data at low energies, as expected for an effective field theory.

2. *Wave functions of Eq. (6)*

The nonzero components of the $\psi_{n>0,\tau}$ bound states are [2,4]

$$\begin{aligned}u_{n,\tau} &= A_{n,\tau}e^{-\sqrt{1-E_{n,\tau}^2}|x-l(x)|}(-1)^n e^{i\tau E_{n,\tau}l(x)},\\ v_{n,\tau} &= -\tau A_{n,\tau}e^{-\sqrt{1-E_{n,\tau}^2}|x-l(x)|}e^{i\left(\frac{\varphi}{2}\right)}e^{-i\tau E_{n,\tau}l(x)},\end{aligned} \tag{11}$$

where

$$l(x) = \begin{cases} x & \text{if } |x| < L/2,\\ \text{sgn}(x)\frac{L}{2} & \text{if } |x| > L/2,\end{cases} \tag{12}$$

and the normalization factor reads as $|A_{n,\tau}| = \{2[L + (1 - E_{n,\tau}^2)^{-1/2}]\}^{-1/2}$. To access the $\psi_{n<0,\tau}$ states, it suffices to apply the Nambu particle-hole transformation $C = \rho_y\tau_y K$. The eigenstates obey the orthogonality relations

$$\int dx\, \psi_{n,\tau}^\dagger(x,\varphi)\psi_{n',\tau}(x,\varphi) = \delta_{\tau,\tau'}\delta_{n,n'} \tag{13}$$

and, if supplemented with the continuum of scattering states, the completeness relation

$$\sum_{n,\tau}\psi_{n,\tau}(x,\varphi)\otimes\psi_{n,\tau}^\dagger(x',\varphi) = \mathbb{I}_{4\times4}\delta(x-x') \tag{14}$$

is respected, where $\mathbb{I}_{4\times4}$ is the 4×4 identity matrix.

For later discussion on the transformation properties of the many-body states under TR, it is convenient to consider the action of $\mathcal{T}_-$ on the above wave functions. The transformation rules may be written as

$$\begin{aligned}i\tau_y\psi_{n,\tau}^*(x,\varphi) &= \tau\psi_{n+\tau,-\tau}(x,-\varphi)\\ &= -\tau\psi_{n,-\tau}(x,2\pi-\varphi).\end{aligned} \tag{15}$$

C. Noninteracting many-particle states

The single-particle wave functions and energies from the previous subsection allow us to construct noninteracting many-particle states in the continuum approximation. This construction will be useful for later discussion on interacting JJs. The starting point is to expand the field operators in terms of ABS as

$$\begin{aligned}\Psi(x) &= \sum_{n,\tau}\psi_{n,\tau}(x,\varphi)a_{n,\tau}(\varphi),\\ a_{n,\tau}(\varphi) &= \int dx\,\psi_{n,\tau}^\dagger(x,\varphi)\Psi(x),\end{aligned} \tag{16}$$

where the operator $a_{n,\tau}$ annihilates the ABS labeled with (n,τ). For the junction length $L \approx \pi\xi_0$ chosen above, we may limit ourselves to the six lowest-energy states

$$|j;\varphi\rangle,\ j = 0,\ldots,5 \tag{17}$$

which are plotted in Fig. 3 and presented in more detail in Appendix A. These states are built from fixing $|0;\varphi=0\rangle$ with all negative-energy single-particle states filled. The excitations over the ground state involve "particle-hole" pairs composed of positive-energy quasiparticles, together with their Nambu conjugate quasiholes. The total number of BdG quasiparticles is the same in all states.

With the states in Eq. (17) and the single-particle energies from the previous subsection, one can build the low-energy many-body spectrum. Alternatively, one can perform a brute-force exact diagonalization of the lattice Hamiltonian in the full many-body Fock space, without any reference to single-particle states. The results of both approaches are depicted in Fig. 3.

On the one hand, we find an excellent agreement between the single-body lattice diagonalization (red dots), where we use $N = 200$ sites, and the many-body numerics (green dashes), where we use $N = 26$. This indicates that the finite-size effects originating from the superconducting leads are not significant. On the other hand, only a fair agreement is obtained between the continuum (black curves) and the lattice numerics. This discrepancy can be tracked down to the φ-dependent contribution of the continuum of scattering states to the ground-state energy [26], which is not captured in the

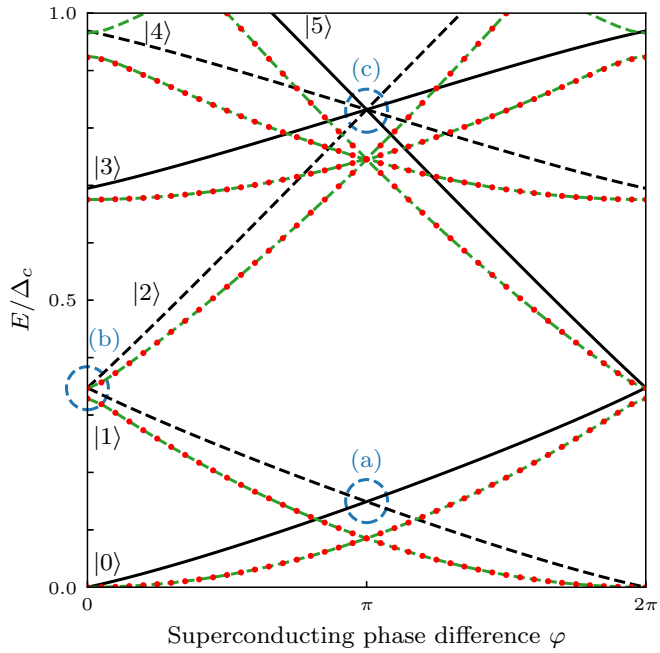

FIG. 3. Many-body energy spectrum in the absence of interactions. The parameter values are the same as in Fig. 2. Black curves are obtained by solving the transcendental equation (7) and by thereafter building many-body energies from Eq. (17); see Appendix A for further details. Full versus dashed black lines correspond to different eigenvalues of the parity operator (22). Contributions from single-particle scattering states are ignored, which generates a mismatch with the remaining data. Red dots correspond to a single-body exact diagonalization of Eq. (1) for chains of $N = 200$ sites, with many-body energies built in a similar way as the black lines from Eq. (17), but scattering states taken into account. Green dashes are also obtained from the lattice Hamiltonian, but from a brute force diagonalization in the many-body Fock space for a chain with $N = 26$ sites. Avoided crossings labeled (b) are due to $\mathcal{T}_-$-breaking terms in the lattice Hamiltonian which become negligible in the $\xi_0 \gg a$ limit (see Fig. 11 of Appendix A).

continuum analysis. A better comparison between the effective theory and the exact diagonalization of the lattice model can be achieved by subtracting off the ground-state energy at each value of φ separately. The obtained excitations energies are physically observable, e.g., in the tunneling density of states [4] or in the microwave response functions evaluated in the next section. When comparing these excitation energies, a much improved agreement is found between the exact diagonalization results and the analytical results (see Fig. 11 in Appendix A).

On a related note, the avoided crossings at $\varphi = 0, 2\pi$ between the states $|1\rangle$ and $|2\rangle$ (cf. the green dashes and red dots in Fig. 3) result from the finite ratio of ξ_0/a leading to the continuum Hamiltonian being only approximately equivalent to the lattice model, with small fast-oscillating $\mathcal{T}_-$-breaking terms lifting Kramers degeneracy. We verified that these anticrossings are eliminated by increasing the ratio of ξ_0/a, which is easily done for single-particle diagonalizations, but not for the many-body case (due to system size limitations).

For the remainder of this section, we study the rich structure of crossings in Fig. 3 from a symmetry point of view. We begin by recalling that TR acting in the second-quantized operators yields [27]

$$\mathcal{T}_-\Psi(x)\mathcal{T}_-^{-1} = i\tau_y\Psi(x). \tag{18}$$

Combining Eqs. (15), (18), and (16), we get

$$\begin{aligned}\mathcal{T}_- a_{n,\tau}(\varphi)\mathcal{T}_-^{-1} &= \tau a_{n+\tau,-\tau}(-\varphi)\\ &= -\tau a_{n,-\tau}(2\pi-\varphi).\end{aligned} \tag{19}$$

Consequently, the action of $\mathcal{T}_-$ on the many-body states of Eq. (A1) at $\varphi = 0$ returns (up to phase factors)

$$\begin{aligned}\mathcal{T}_-|0;0\rangle &\sim |0;0\rangle,\\ \mathcal{T}_-|1;0\rangle &\sim |2;0\rangle,\\ \mathcal{T}_-|3;0\rangle &\sim |3;0\rangle,\end{aligned} \tag{20}$$

with the other states being either invariant or having partners at higher energies. At $\varphi = \pi$, one gets

$$\begin{aligned}\mathcal{T}_-|0;\pi\rangle &\sim |1;\pi\rangle,\\ \mathcal{T}_-|2;\pi\rangle &\sim |5;\pi\rangle,\\ \mathcal{T}_-|3;\pi\rangle &\sim |4;\pi\rangle.\end{aligned} \tag{21}$$

These transformations demonstrate that many of the crossings in the spectrum of Fig. 3 are protected by the effective TR invariance of the low-energy physics (or the true TR invariance of the QSH edge modes, in the case of a QSH JJ). Yet, some of the crossings therein are protected by another symmetry as well, namely, the local fermion parity. The local fermion-parity operator counts the parity of the number of ABS excitations in the many-body state. It can be written as

$$P_{\text{in}}(\varphi) \equiv (-1)^{(a_{0,+}^\dagger a_{0,+} + \sum_{n>0,\tau} a_{n,\tau}^\dagger a_{n,\tau})}, \tag{22}$$

where the sum over n is done among the discrete-energy bound states only ($n = 1$ only, for our parameter values).[1] An application of this operator over the many-body states written explicitly in Eq. (A1) returns the pattern of full and dashed black curves displayed in Fig. 3. Importantly, P_{in} is conserved at every φ as long as the total fermion parity of the system is conserved.

The conservation of P_{in} and TR allows to understand the various crossings in Fig. 3. At $\varphi = 0$, $|1;0\rangle$ and $|2;0\rangle$ have the same parity and are related by TR symmetry; they constitute Kramers partners. At $\varphi = \pi$, TR operation connects states of opposite parity. Accordingly, the degeneracy between $|0;\pi\rangle$ and $|1;\pi\rangle$ (two states of opposite parity) is protected by both TR symmetry and the conservation of P_{in}. Indeed, in the

[1]This definition of the parity operator is not unique. The modes contributing to it must be spatially localized in the weak link and the number of such modes depends on the length of the link. Also, in the absence of TR-breaking perturbations, the connection of the ABS modes with the continuum of scattering dictates that a cutoff must be introduced, in a rather arbitrary way, in the mode sum, depending on φ. Finally, the definition is sensitive to the choice of the reference ground state. The form displayed in this work is in accordance with our conventions, but may be straightforwardly adjusted to other conventions.

topological phase, the parity eigenvalues of the two lowest-energy many-body states are inverted when going from $\varphi = 0$ to 2π, which requires a band crossing in-between.

The higher-energy fourfold crossing at $\varphi = \pi$ is only partly protected. On the one hand, the degeneracy between $|2;\pi\rangle$ and $|5;\pi\rangle$, as well as the degeneracy between $|3;\pi\rangle$ and $|4;\pi\rangle$, are enforced by both TR symmetry and the conservation of P_{in}. On the other hand, the degeneracy between $|2;\pi\rangle$ and $|3;\pi\rangle$ is "accidental" and guaranteed only at the noninteracting level. Indeed, we will show below that TR- and parity-preserving interactions introduced at the lattice level break the fourfold degeneracy into a pair of twofold crossings, as previously proposed in the context of QSH JJ [1–5].

D. Fractional Josephson effects: Phenomenology

Having understood the low-energy spectrum of the noninteracting junction, it is useful to embark on a pedagogical discussion of the different fractional Josephson effects listed in the Introduction. The different effects can be distinguished by focusing on the several crossings that take place in the energy spectrum of Fig. 3, at $\varphi = n\pi$ ($n \in \mathbb{Z}$). To guide the explanation, we use the labels "(a)" for the lowest twofold crossing at $\varphi = \pi$, "(b)" for the lowest twofold crossings at $\varphi = 0$, and "(c)" for the fourfold crossing at $\varphi = \pi$.

When all (a), (b), and (c) crossings are preserved (like in Fig. 3), the ABS energy levels are continuously connected, as a function of φ, with the continuum of scattering states of energies greater than Δ_c. As a consequence, dc-voltage biasing the junction leads to a time-dependent evolution of the states that eventually connects the ground state with the continuum of scattering states, thereby generating a dissipative dc contribution on top of a 2π-periodic Josephson current [1,2]. In order to have only the purely ac component of the Josephson current, it is necessary to disconnect the ABS from the continuum by opening a gap either at (a), (b), or (c).

The crossing at (a) is gapped in topologically trivial JJs, which lack MZMs and do not have the corresponding conserved local fermion parity. Accordingly, the lowest curve in Fig. 3 fully separates from the rest. The evolution of this state as function of φ is 2π periodic, corresponding to a standard, dissipationless, Josephson effect.

A second possible scenario involves lifting the crossing (b). Since this crossing is protected by TR symmetry alone, it can be gapped by applying a magnetic perturbation on the QSH JJ [3] or by a adding potential barrier (which breaks $\mathcal{T}_-$ symmetry) in the Kitaev chain JJ. The gap scales with the strength of the TR-breaking perturbation, which is responsible for localizing the Majorana modes at the boundaries of the weak link. Due to this gap, a doublet of states [the crossing at (a) being protected by P_{in} conservation] becomes disconnected from the remaining states, including the scattering ones, and the 4π-periodic fractional Josephson effect arises. This effect is characteristic of weakly hybridized MZMs allowing for single-electron tunneling through the junction.

The third and last scenario arises from lifting the fourfold degeneracy at (c). This crossing, composed of states with one- and two-quasiparticle excitations, exists only if the JJ can accommodate at least three discrete ABS levels with energies smaller than Δ_c (cf. Fig. 2). TR- and P_{in}-conserving interactions can lift this fourfold crossing in two pairs of TR- and parity-protected crossings. In a QSH JJ, umklapp interactions (at half-filling) or interactions with magnetic impurities (at any filling) are known to lift the fourfold degeneracy [2,4,5,10,12,15]. The case of an interacting Kitaev chain JJ will be discussed below. The consequence of the gap opening at (c) is an 8π-periodic fractional Josephson effect characterized by transport of charges $e/2$ through the junction.

E. T-breaking perturbations

In this section, we consider a junction where the effective TR symmetry $\mathcal{T}_-$ is broken and the 4π-periodic Josephson effect arises. This can be achieved in several ways but, to keep the analogy with the QSH JJ interrupted by a magnetic insulator, we choose to implement a potential barrier inside the junction,

$$H_{SB} = \delta\mu \sum_{l>-N_L/2}^{N_L/2-2} c_l^\dagger c_l. \tag{23}$$

For more appreciable effects, we take the perturbation to be larger than the bandwidth ($\delta\mu > t$). This term transforms the normal weak link into a trivial insulator and thereby localizes Majorana modes at the edges of each SC bank, which hybridize perturbatively. From the point of view of our continuum theory, H_{SB} leads to single-body backscattering between the left and right movers, violating the effective TR symmetry.

In order to make a seamless connection with the interacting case discussed in the next subsection, we perform an exact diagonalization of the noninteracting TR-broken junction in the many-body Fock space. As the lattice Hamiltonian preserves the total fermion parity, we project the Fock space into the subspace of an even total number of fermions. As seen in Fig. 4(a), the subgap part of the spectrum is disconnected from the scattering states, leaving the blue and orange bands as the ground-state doublet. As expected, the avoided crossing happens at the crossing (b) of the spectrum of Fig. 3.

The continuation of the coloring through the crossings at $\varphi = \pi$ and 3π in Fig. 4(a) is justified by the the conservation of P_{in} [cf. Eq. (22)]. This form of the parity operator cannot be easily accessed from the many-body exact diagonalization, which circumvents the single-particle energy levels.

To verify the protection of the crossings, we consider instead the parity of occupation of a nonlocal state built out of the MZMs Γ_L and $\Gamma_R(\varphi)$ located, respectively, at the left and right *outer* ends of the chain [13]. Since the parity of the total number of fermions has been fixed, the parity of this nonlocal outer mode, with operator corresponding to[2]

$$P_{\text{out}}(\varphi) = i\Gamma_L\Gamma_R(\varphi), \tag{24}$$

[2]In the particular case of a perfectly dimerized fine-tuned Kitaev chain ($\mu = 0$, $\Delta_0 = t$), MZMs are localized on single sites and the parity operator is simply $P_{\text{out}} = (c_{N/2-1}e^{i\varphi/2} + c_{N/2-1}^\dagger e^{-i\varphi/2})(c_{-N/2}^\dagger - c_{-N/2})$. Away from this point, MZMs extend over several lattice sites [see Eq. (14) from Ref. [13], and also Ref. [35]] and the expression for P_{out} becomes less simple.

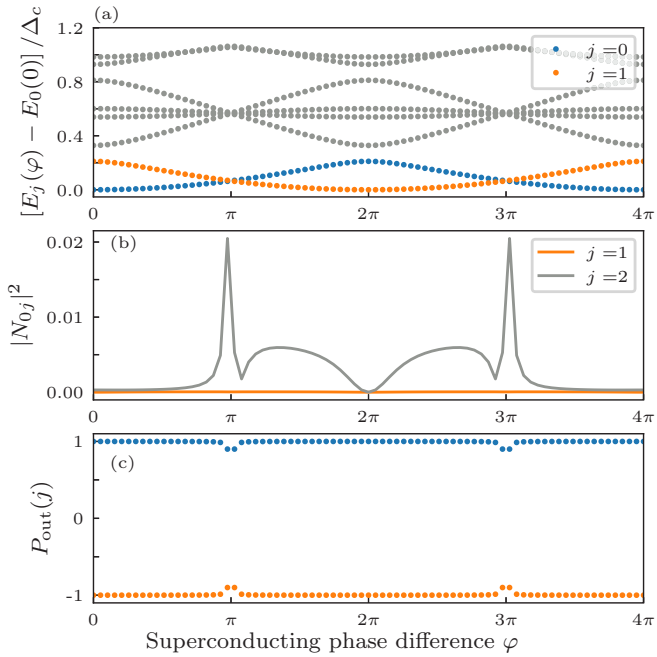

FIG. 4. Exact diagonalization of a noninteracting Kitaev chain JJ with broken effective TR. The parameter values are $\mu = 0$, $\Delta_0 = t/2$, $N_L = 8$, $N = 26$, $\delta\mu/t = 1.3$. (a) Many-body spectrum. The blue and orange curves form the ground-state multiplet. Gray states are excited states. (b) Off-diagonal matrix elements of the total number operator $\hat{N}$ for the lowest many-body states. The vanishing of $N_{01}(\varphi)$ follows the conservation of the local fermion parity in (c). (c) The parity of occupation of the nonlocal fermion in Eq. (24) for the states forming the ground-state multiplet. Parity conservation protects the crossings in the ground-state doublet and enforces the 4π periodicity of the blue and orange states in (a).

is locked to the value of $P_{\rm in}$ in Eq. (22). In the thermodynamic limit, where each superconducting bank is sufficiently long, the MZM operators are well localized and commute with the lattice Hamiltonian (1) even when the JJ is strongly interacting. Thus, for N sufficiently large, the states $|j;\varphi\rangle$ are eigenstates of $P_{\rm out}(\varphi)$.

The computation of the expectation value $P_{{\rm out},i}(\varphi) \equiv \langle i;\varphi|P_{\rm out}|i;\varphi\rangle$ returns Fig. 4(c), showing that the parity is conserved and continuously defined for the blue and orange ground doublet across the full 4π evolution. The small kinks close to $\varphi = \pi, 3\pi$ are finite-size effects that should vanish for larger values of N. Consequently, the crossings are protected and the 4π Josephson effect develops.

From the many-body spectrum and wave functions, we can obtain matrix elements of physical observables. With the cQED applications of the next section in mind, let us consider $N_{ij}(\varphi) \equiv \langle i;\varphi|\hat{N}|j;\varphi\rangle$, the matrix elements of the total number of particles $\hat{N} = \sum_i c_i^\dagger c_i$. Figure 4(b) displays N_{0j}, where the state $i = 0$ corresponds to the blue state in Fig. 4(a). Since the total number of particles is a sum over local operators, it cannot connect states with different values of the nonlocal operator $P_{\rm out}$. This is why $N_{01}(\varphi)$ and $N_{02}(\varphi)$ vanish.[3] In contrast, N_{03} is nonzero because the state $j = 3$ has the same parity as $j = 0$ and can thus be connected by a local and parity-preserving operator such as $\hat{N}$.

F. Short-range Coulomb interactions

The previous subsections have established the equivalence between the low-energy properties of the QSH JJ and the Kitaev chain JJ at the noninteracting level. Here, we incorporate to the Hamiltonian (1) the simplest possible interaction term, a first-neighbor extended Hubbard interaction inside the normal region of the junction

$$H_{EH} = V \sum_{l=-N_L/2}^{N_L/2-2} n_l n_{l+1}. \tag{25}$$

Outside the junction, the proximity coupling to a three-dimensional superconductor is assumed to screen away the interactions.

In the continuum approximation, the extended Hubbard interactions decompose into

$$\begin{aligned}\frac{c_n^\dagger c_n}{a}\frac{c_{n+1}^\dagger c_{n+1}}{a} \approx{}& \rho(x)\rho(x+a) + [e^{i2k_F a}(\psi_R^\dagger\psi_L)(x)(\psi_L^\dagger\psi_R)(x+a) + \text{H.c.}] \\ &+ [e^{-i2k_F(2x+a)}(\psi_R^\dagger\psi_L)(x)(\psi_R^\dagger\psi_L)(x+a) + \text{H.c.}] \\ &+ \{e^{-i2k_F x}[e^{-i2k_F a}\rho(x)(\psi_R^\dagger\psi_L)(x+a) + (\psi_R^\dagger\psi_L)(x)\rho(x+a)] + \text{H.c.}\},\end{aligned} \tag{26}$$

where $\rho(x) =: \psi_R^\dagger\psi_R : (x) + : \psi_L^\dagger\psi_L : (x)$ and the colons indicate normal ordering. The terms in Eq. (26) coincide with those one would write for an interacting QSH edge with TR symmetry. This establishes the equivalence between the QSH JJ and the Kitaev chain JJ at the interacting level. The first nonoscillating terms on the right-hand side of Eq. (26) are known to renormalize the velocities of left- and right-moving fermions [28], without opening spectral gaps. The second line of Eq. (26) (umklapp/pair-backscattering terms) and the third line (Friedel oscillating terms) are rapidly oscillating

[3]The computed values of $N_{01}(\varphi)$ are $O(10^{-3})$ for our parameters of choice. We performed a finite-size scale analysis of this quantity and found that it decreases in an oscillatory way, enveloped by a monotonically decaying function. This suggests that, in the thermodynamic limit (where there is no overlap between the well-localized inner and outer MZMs), $N_{01}(\varphi)$ vanishes, with the local fermion parity a fully well-defined quantum number at low energies.

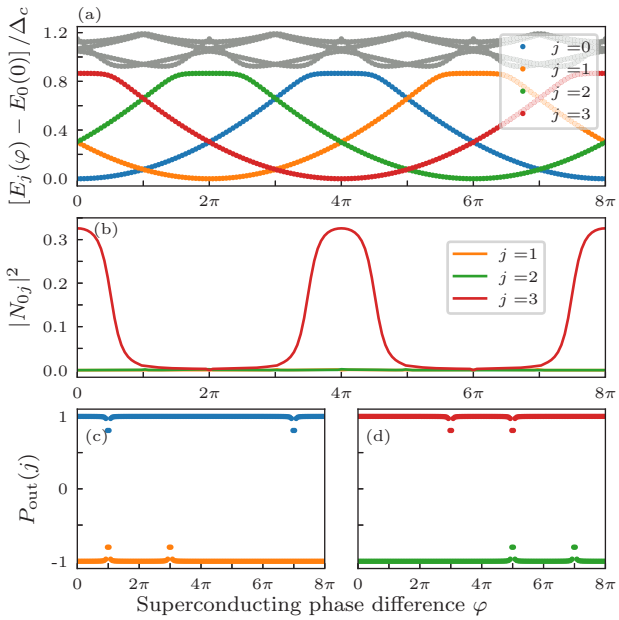

FIG. 5. Exact diagonalization of the interacting Kitaev chain JJ. The parameter values are $\mu = 0$, $\Delta_0 = t/2$, $N_L = 8$, $V = 2t$, and $N = 26$. (a) Many-body spectrum. Colored states form the fourfold ground-state multiplet. Gray states are excited states. (b) Off-diagonal matrix elements of the total number operator $\hat{N}$ between the $i = 0$ (blue) band and the rest of the states forming the ground-state multiplet. The matrix elements between states of opposite local fermion parity vanish. The matrix elements between states of the same parity are nonzero, except when they cross. At the crossing points, the effective TR symmetry enforces the vanishing of the matrix element of $\hat{N}$. (c) Parity of occupation of the nonlocal fermion in Eq. (24) for the states forming the ground-state multiplet.

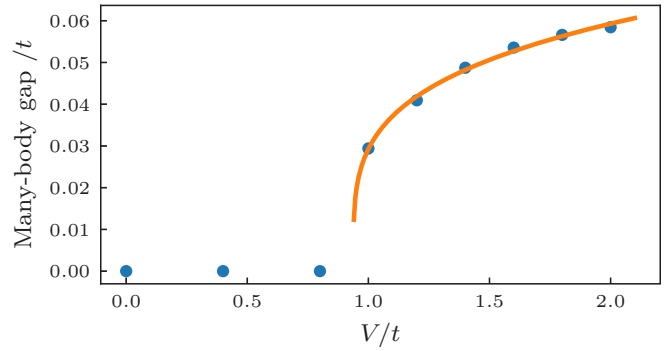

FIG. 6. Many-body gap of the interacting Kitaev chain JJ, calculated by exact diagonalization (blue disks). The parameter values are $\mu = 0$, $\Delta_0 = t/2$, $N_L = 8$, and $N = 26$. The gap scales as $\sim (V - V_c)^\gamma$, where V_c is the critical interaction strength for the gap opening. $V_c \simeq (0.94 \pm 0.02)t$, and $\gamma \simeq (0.25 \pm 0.03)$ are obtained from a power-law fit of the numerical data (orange solid curve).

away from $\mu = 0$ and $\pm 2t$, respectively. In perturbative renormalization group analyses, only the umklapp terms at half-filling ($\mu = 0$) are seen to lead to a strong-coupling flow that indicates a gap opening in the low-energy degrees of freedom.

Figure 5(a) displays the energy dispersion as a function of φ for the eight lowest-energy many-body states, obtained from exact diagonalization. The blue, orange, green, and red curves form the ground-state multiplet, separated from the excited states (in gray) by a many-body gap. This gap develops at the fourfold crossing of Fig. 3 and scales as $\sim (V - V_c)^\gamma$, with $V_c/t \simeq 0.94$ and $\gamma \simeq 0.25$ obtained by a power-law fit of the numerical data (see Fig. 6).

We remark that $V/t > 1$ is a strong interaction regime, likely hard to achieve in real systems. Also, even in this strong-coupling regime, the many-body gap is a small fraction of the bandwidth. We have checked numerically that the many-body gap is not reduced when $\mu \neq 0$. At first sight, this finding is surprising from the point of view of a perturbative analysis. One possible explanation is that the gap may be originating from oscillatory umklapp or Friedel terms because these oscillations are not sufficiently fast to average out in our weak links of mesoscopic size. Another possible explanation is that the perturbative arguments arguing for the irrelevance of the oscillatory Friedel and umklapp terms break down in the strong-coupling regime, where the interaction strength exceeds the bandwidth.

The colors in Fig. 5(a) are in one-to-one correspondence with the mean values of $P_{\rm out}$ in Figs. 5(c) and 5(d). This parity conservation protects the band crossings at $\varphi = \pi \mod 2\pi$, while the crossings at $\varphi = 0 \mod 2\pi$ are preserved by TR symmetry. Thus, the ground-state multiplet is 8π periodic and so is the Josephson effect. In anticipation to the next section, let us once again consider the off-diagonal elements of the total number operator $\hat{N}$ for the states belonging to the ground-state multiplet, as displayed in Fig. 5(b). The fact that $N_{01}(\varphi) \simeq N_{02}(\varphi) \simeq 0$ for all values of φ can be attributed to the conservation of the local fermion parity. Indeed, the extended Hubbard interactions, which act again locally and only inside the weak link, commute with $P_{\rm out}$. In contrast, $N_{03}(\varphi)$ is finite for all values of φ away from $\varphi = 2\pi \mod 4\pi$ because the states $j = 0$ and 3 carry the same parity. The crossings between $j = 0$ and 3 are, however, still protected by the effective low-energy TR symmetry $\mathcal{T}_-$, and that translates into the vanishing of $N_{03}(\varphi)$ at $\varphi = 2\pi, 6\pi$.

III. FRACTIONAL JOSEPHSON EFFECTS IN CQED ARCHITECTURES

Due to their high sensitivity, flexibility, and noninvasive probing, cQED platforms have been proposed for the study and detection of topological phases in Josephson junctions [17–19]. The general approach of cQED, as illustrated in Fig. 7, consists of two steps: (i) the placement of the circuit one wishes to study inside a cavity resonator and (ii) the measurement of reflectances and transmittances between input and output microwave modes inserted in the cavity through a waveguide. The in/out modes couple to the cavity photons, whose dynamics is in turn influenced by the dynamics of the circuit of interest.

In this section, we present an exact diagonalization calculation of certain cQED observables in a topological JJ. Our study goes beyond earlier theoretical works by incorporating strong short-range Coulomb interactions, crucial for the emergence of the 8π-periodic Josephson effect.

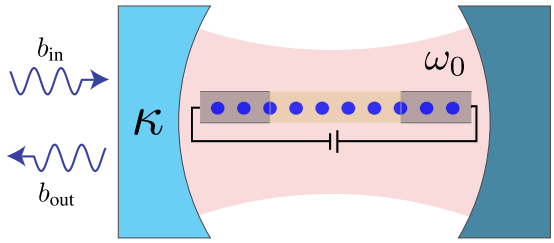

FIG. 7. Cartoon of a cQED architecture. A cavity resonator of frequency ω_0 and linewidth κ_0 contains an interacting topological JJ. The cavity is partially transmitting on a single side, so that it can be probed by input/output fields.

A. Input/output formalism

We consider a Hamiltonian with three components: probing fields, a cavity, and a topological Josephson junction:

$$H = H_S + H_I + \omega_0 a^\dagger a + \sum_n \Omega_n b_n^\dagger b_n - i\sum_n \lambda_n (a^\dagger b_n - a b_n^\dagger). \quad (27)$$

Here, $a^{(\dagger)}$ and $b_n^{(\dagger)}$ are the annihilation (creation) operators for cavity photons and the mode n of the probing field, respectively; Ω_n and λ_n are the frequencies of the probe fields and the cavity-probe coupling constants, respectively; ω_0 is the resonance frequency of the empty cavity. The Hamiltonian H_S describes the JJ,

$$H_S = H_{\text{JJ}}(\varphi) + H_\alpha, \quad (28)$$

where $\alpha = SB$ [cf. Eq. (23)] or EH [cf. Eq. (25)], depending on whether we are dealing with the $\mathbb{Z}_2$ or $\mathbb{Z}_4$ fractional Josephson effect. Also, we consider a capacitive coupling between the junction and cavity,

$$H_I = g\hat{N}(a + a^\dagger), \quad (29)$$

where g is a coupling constant, and $\hat{N} = \sum_i c_i^\dagger c_i$ is the total number operator.

The dynamics of the cavity fields can be obtained by the standard input/output formalism [29], yielding

$$\dot{\tilde{a}}(t) = -i[\tilde{a}(t), \tilde{H}_I] - \left(i\omega_0 + \frac{\kappa_0}{2}\right)\tilde{a}(t) + \sqrt{\kappa_0}\tilde{b}_{\text{in}}(t). \quad (30)$$

Here, tildes denote operators written in the Heisenberg picture, κ_0 is the cavity damping constant due to the coupling with the probe, and

$$\tilde{b}_{\text{in}}(t) \equiv \sum_n \lambda_n \tilde{b}_n(t_0) e^{-i\Omega_n(t-t_0)} \quad (31)$$

is the input field with t_0 a reference time. In Eq. (31), the sum over the modes is constrained to $\Omega_n \approx \omega_0$. The input field is related to the output field b_{out} by the boundary condition

$$\tilde{b}_{\text{in}}(t) + \tilde{b}_{\text{out}}(t) = \sqrt{\kappa_0}\tilde{a}(t). \quad (32)$$

When b_{in} is used to drive the cavity, the readout of b_{out} enables to measure the cavity frequency and linewidth. The commutator in Eq. (30) forecasts that the dynamics of the junction will be intertwined with that of the cavity. To second order in g and in the rotating-wave approximation, Eq. (30) becomes (cf. Appendix B)

$$\dot{\tilde{a}}(t) = -\left(i\omega_R + \frac{\kappa_R}{2}\right)\tilde{a}(t) + \sqrt{\kappa_0}\tilde{b}_{\text{in}}(t) - igN^i(t), \quad (33)$$

where $\omega_R = \omega_0 + \bar{\omega}(\varphi)$ and $\kappa_R = \kappa_0 + \bar{\kappa}(\varphi)$ are the renormalized cavity frequency and linewidth, whereas $N^i(t)$ is the number operator in the interaction picture. Thus, the junction induces a φ-dependent pull $\bar{\omega}(\varphi)$ in the resonance frequency of the cavity, in addition to a φ-dependent change $\bar{\kappa}(\varphi)$ in the cavity linewidth [19]. The explicit expressions for $\bar{\omega}(\varphi)$ and $\bar{\kappa}(\varphi)$ are shown below. The last term in Eq. (33) is an extra driving term for the cavity which, as shown in Appendix B, may be ignored because it contributes only at zero frequency.

The fractional Josephson effects manifest themselves in the φ dependence of ω_R and κ_R. If the rate at which φ is varied is faster than all the energy relaxation rates of the quasiparticles but smaller than the topological energy gap, ω_R and κ_R are 4π- (8π-) periodic functions of φ when the junction hosts a $\mathbb{Z}_2$ ($\mathbb{Z}_4$) Josephson effect. One way to realize this condition is through the application of an appropriate dc voltage bias V across the junction, under which $\varphi = \varphi_0 + 2eVt/\hbar$ evolves with time t. In the remainder of this section, we compute $\bar{\omega}(\varphi)$ and $\bar{\kappa}(\varphi)$ and propose an experiment to capture their anomalous periodicities via the input/output fields.

B. Cavity frequency pull

At zero temperature, the expression for the cavity frequency pull reads as (cf. Appendix B)

$$\bar{\omega}(\varphi) = 2g^2 \sum_{j\neq 0} |N_{0j}(\varphi)|^2 \frac{\Delta E_{0j}(\varphi)}{(\Delta E_{0j}(\varphi))^2 - \omega_0^2}, \quad (34)$$

where $\Delta E_{0j}(\varphi) = E_0(\varphi) - E_j(\varphi)$, $N_{0j}(\varphi) = \langle 0;\varphi|\hat{N}|j;\varphi\rangle$, and $|0;\varphi\rangle$ is the many-body state whose energy is the lowest of all when $\varphi = 0$ [the blue band in either Fig. 4(a) or Fig. 5(a)]. Replacing the state $|0;\varphi\rangle$ by any other states in the ground-state multiplet amounts to an inconsequential shift of φ by a multiple of 2π in Eq. (34). The sum in j is over all other states, scattering states included. In our numerical calculations, we truncate the sum to the eight lowest-energy many-body states.

Figure 8 displays $\bar{\omega}(\varphi)$ for JJs hosting $\mathbb{Z}_2$ and $\mathbb{Z}_4$ Josephson effects. The cavity frequency pull is either 4π or 8π periodic in φ. For the 8π scenario, $\bar{\omega}$ can actually become positive, in contrast with the 4π-periodic case. The origin of this difference comes from transition matrix elements between states of the same local fermion parity. In JJs hosting the $\mathbb{Z}_4$ Josephson effect, the fact that $N_{03}(\varphi) \neq 0$ for generic φ and $\Delta E_{03}(\varphi) > 0$ for certain intervals of φ (cf. Fig. 5) is responsible for $\bar{\omega}(\varphi) > 0$ in those intervals. This situation is not realized in JJs that host the $\mathbb{Z}_2$ Josephson effect, where the conservation of the local fermion parity forbids transitions with $\Delta E_{0j} > 0$.

We note in passing that the capacitive coupling we consider here describes a junction fully embedded in a cavity. Other possibilities exist, like coupling only either side of the junction, the remaining side being grounded, or even coupling only to the number of electrons inside the weak link. We find that the largest contributions to the cavity pull come from couplings around the weak-link region, which is also the

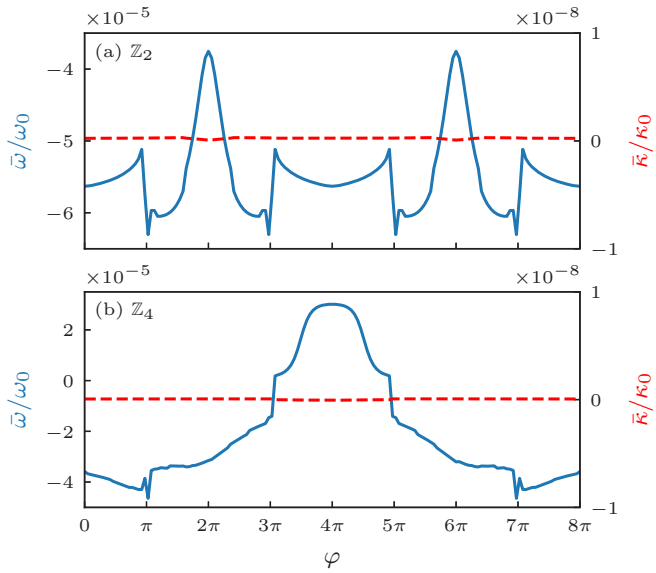

FIG. 8. Renormalization of the cavity resonance frequency (blue, full lines) and linewidth (red, dashed lines), calculated by exact diagonalization of the Kitaev chain JJ at $V = 2t$. (a) Noninteracting JJ with broken time-reversal symmetry. (b) Interacting JJ with time-reversal symmetry. The bare cavity resonance frequency is chosen as $\omega_0 = 4 \times 10^{-3}\Delta_c$, parametrically smaller than the energy gaps separating the ground-state multiplets from the excited states. The broadening of the delta functions in Eq. (35) is taken to be of the order of the bare cavity linewidth $\kappa_0 \simeq 10^{-3}\omega_0$. For the cavity-junction coupling strength, we use $g = \omega_0/10$ [30]. The periodicity of the cavity pull in the superconducting phase difference follows that of many-body wave functions of the problem. When ω_0 is large compared to the disorder broadening of the ABS, but smaller than the energy gaps separating the ground-state multiplet from the excited states, the conservation of the local fermion parity (as well as time-reversal symmetry, in the case of the $\mathbb{Z}_4$ Josephson effect) results in a negligible renormalization of the cavity linewidth.

region that is not screened from electromagnetic interactions by the SC leads. Qualitatively, our analysis is preserved as long as the weak-link region contributes to the coupling.

C. Cavity linewidth renormalization

At zero temperature, the renormalization of the cavity linewidth is given by

$$\bar{\kappa}(\varphi) = 4\pi g^2 \sum_{j\neq 0} |N_{0j}(\varphi)|^2 [\delta(\Delta E_{0j}(\varphi) + \omega_0) - \delta(\Delta E_{0j}(\varphi) - \omega_0)]. \quad (35)$$

The Dirac deltas are to be broadened into Lorentzians by effects such as disorder and feedback of the cavity dynamics into the junction energies, which will be considered here only phenomenologically.[4]

[4]More sophisticated treatments of disorder have been employed recently, but only for noninteracting junctions; see, e.g., M. Trif, O. Dmytruk, H. Bouchiat, R. Aguado and P. Simon, Phys. Rev. B **97**, 041415(R) (2018).

The values of $\bar{\kappa}$ calculated by exact diagonalization are presented in Fig. 8 (red dashed lines). Importantly, when ω_0 is large compared to the disorder broadening of the ABS but smaller than the TR-breaking gap from $\delta\mu$ or the TR-preserving gap due to interactions (a circumstance believed to be realistic), we find $\bar{\kappa} \simeq 0$. This null result has a simple explanation. Because ω_0 is small compared to typical ABS energy scales, the Dirac delta functions in Eq. (35) are satisfied only very close to the crossings. But, the matrix elements of $N_{0j}(\varphi)$ are vanishingly small at the crossings, due to the conservation of either the local fermion parity or time reversal.

D. Phase shift

Having found how the topological JJ influences key physical properties of the cavity, we now focus on how to access these. The Fourier transform of Eq. (33) and the boundary conditions in Eq. (32) allow to relate the outgoing signal and incoming signals in a single-sided partially transparent cavity. Neglecting zero-frequency contributions, we obtain

$$\langle \tilde{b}_{\rm out}(\omega)\rangle = re^{i\alpha}\langle \tilde{b}_{\rm in}(\omega)\rangle, \quad (36)$$

where r is the reflection coefficient obeying

$$r^2 = \frac{(\omega-\omega_R)^2 + \left(\frac{\kappa_0-\bar{\kappa}}{2}\right)^2}{(\omega-\omega_R)^2 + \left(\frac{\kappa_R}{2}\right)^2} \quad (37)$$

and

$$\alpha = \arg\left[(\kappa_0^2 - \bar{\kappa}^2)/4 - (\omega-\omega_R)^2 + i\kappa_0(\omega-\omega_R)\right] \quad (38)$$

is the phase shift. The quantities r and α are directly measurable in experiments. As $\bar{\kappa} = 0$ (cf. preceding subsection), $r^2 = 1$ for all values of φ. Hereafter, we concentrate on α.

Figure 9 shows the behavior of α as function of φ at frequencies around ω_0. The phase shift changes sign as the frequency of the probe crosses the resonance frequency. This enables a precise determination of ω_R and its anomalous periodicity through reflectrometry measurements.

One approach to carry out the experimental verification of Fig. 9 consists of the following steps: (1) Measure α as a function of the probing frequency ω in the absence of current and bias voltages. The value of ω at which α changes sign constitutes ω_R at $\varphi = 0$. (2) Choose a window of frequency $\delta\omega_0$ around the $\varphi = 0$ value of ω_R. For each value of frequency inside this window, let φ evolve in time while continuously measuring α. The phase evolution is best accomplished by a dc-voltage bias V, under which $\dot{\varphi} = 2eV/\hbar$ is constant. This has the advantage of knowing how much φ has wound in a given measurement time, thereby allowing to extract the periodicity of α in φ.

In order to observe the anomalous periodicities, the measurement time in step (2) must be shorter than the energy relaxation rate, longer than $4\pi\hbar/(eV)$ (so that the phase winds at least by 8π), and much longer than the inverse of the data acquisition rate (which is $\simeq$1 ns in state-of-the-art experiments [31]). In addition, $2eV$ must be smaller than (i) the energy gap separating the ground-state multiplet from the excited states (to avoid Landau-Zener tunneling away from the ground state), and (ii) $\hbar\omega_0$ (to prevent that the inelastic tunneling of Cooper pairs generates photons at the

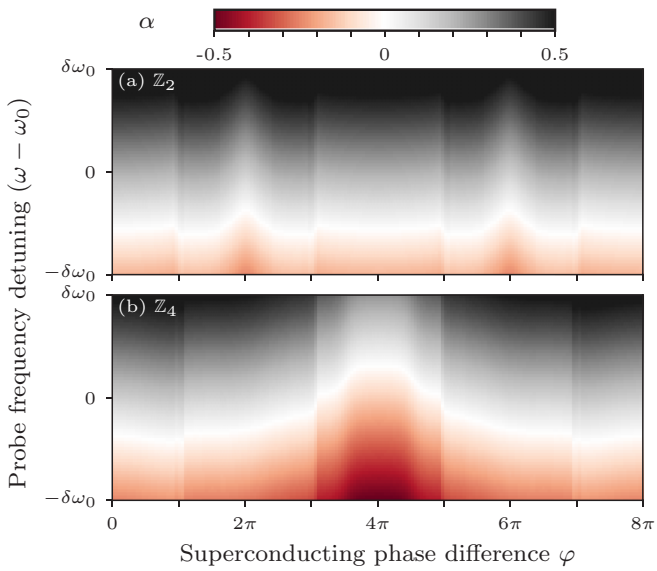

FIG. 9. Phase shift $\alpha(\omega)$ between input and output signals for a single-sided cavity containing a Kitaev chain JJ. We show α for $\omega \in (\omega_0 - \delta\omega_0, \omega_0 + \delta\omega_0)$, where ω_0 is the resonance frequency of the empty cavity and $\delta\omega_0 = 10^{-1}\kappa_0$. Top panel: noninteracting JJ with broken time-reversal symmetry. Bottom panel: interacting JJ with time-reversal symmetry.

cavity's frequency). All of these conditions are simultaneously satisfiable in view of recent reports [20] of long ($\simeq$0.1 ms) energy relaxation times in Al-coated InAs nanowires.

IV. SUMMARY AND CONCLUSIONS

We have presented an exact diagonalization study of fractional Josephson effects in interacting topological Josephson junctions (JJs). By a careful comparison with a continuum low-energy version of the problem, we have established that JJs created out of Kitaev chains can be used to simulate JJs created at the edges of quantum spin Hall insulators. Central to this equivalence is an emergent time-reversal symmetry squaring to -1 in the low-energy description of the lattice problem. The existence of this effective symmetry is contingent on (i) the expansion of fermionic field operators around the two normal-state Fermi points, located at wave vectors $\pm k_F$ and (ii) $\xi_0 k_F \gg 1$, where ξ_0 is the superconducting coherence length. These conditions allows to neglect oscillating terms that would otherwise break the effective time-reversal symmetry. These two conditions are readily satisfied deep in the topological phase of Kitaev chains, provided that the junction is, in sum, perfectly transparent. They, however, fail as one approaches the phase transition toward the trivial phase, as k_F becomes gradually smaller, vanishing at the critical point. In sum, given the absence of a Fermi surface in the trivial regime, the effective time-reversal symmetry is an attribute of Kitaev chains in the topological phase.

The use of Kitaev chain JJs to simulate quantum spin Hall JJs offers two advantages. First, it extends the 8π-periodic Josephson effect to systems other than quantum spin Hall insulators, where it was originally proposed. In this regard, the ongoing advances towards the engineering of Kitaev chains [32–34], together with gate-tuned transparencies of up to 98% reported in Al-coated InAs nanowires [20], presage the realization of Kitaev chain JJs of high transparency.

Another advantage of our lattice simulations is that they give access to physical observables that are difficult to compute using continuum analytical approaches from earlier works. To illustrate this point, we have considered an interacting Josephson junction coupled to a microwave resonator and have calculated the renormalizations of the cavity's resonance frequency and linewidth. We have found that the cavity linewidth is approximately unchanged by the presence of the junction for a reasonable range of physical parameters, while the cavity frequency displays 4π- and 8π-periodic features that may be accessed by measuring the phase shift between incoming and outgoing signals.

For future work, it will be interesting to investigate signatures of the $\mathbb{Z}_2$ and $\mathbb{Z}_4$ Josephson effects in higher-order photon correlation functions.

ACKNOWLEDGMENTS

We thank D. Sénéchal, V. L. Quito, J. Teo, B. Douçot, P. Ghaemi, R. Pereira, J.O. Simoneau, B. Reulet, and F. Zhang for insightful discussions and suggestions. This research has been financed by the Canada First Research Excellence Fund, the Natural Science and Engineering Council of Canada, and the Fonds de Recherche du Québec Nature et Technologies. Numerical calculations were done with computer resources from Calcul Québec and Compute Canada.

APPENDIX A: SINGLE-PARTICLE MANY-BODY STATES

The knowledge of the single-particle Andreev bound states allows for an explicit construction of noninteracting low-energy many-body states. Without applying the Nambu constraint, these many-body states are obtained by the introduction of positive-energy particles and destruction of their corresponding negative-energy particle-hole symmetric partners. The first six states read as

$$
\begin{aligned}
|0;\varphi\rangle &= \left[\prod_{n<0} a^\dagger_{n,+}\right]\left[\prod_{n<0} a^\dagger_{n,-}\right][a^\dagger_{0,-}]|\Omega_e\rangle,\\
|1;\varphi\rangle &= a^\dagger_{0,+}a_{0,-}|0;\varphi\rangle,\\
|2;\varphi\rangle &= a^\dagger_{1,-}a_{-1,+}|0;\varphi\rangle,\\
|3;\varphi\rangle &= a^\dagger_{1,-}a^\dagger_{0,+}a_{-1,+}a_{0,-}|0;\varphi\rangle,\\
|4;\varphi\rangle &= a^\dagger_{1,+}a_{-1,-}|0;\varphi\rangle,\\
|5;\varphi\rangle &= a^\dagger_{1,+}a^\dagger_{0,+}a_{-1,-}a_{0,-}|0;\varphi\rangle,
\end{aligned}
\tag{A1}
$$

where $|\Omega_e\rangle$ is the nonsuperconducting electron Fermi sea and the φ dependence of the operators has been omitted. These states are pictorially represented in Fig. 10.

To incorporate the Nambu constraint, we have to define a reference set of operators and enforce the particle-hole operation

$$
\mathcal{C}\Psi(x)\mathcal{C}^{-1} = \rho_y\tau_y[\Psi^\dagger(x)]^T = \Psi(x). \tag{A2}
$$

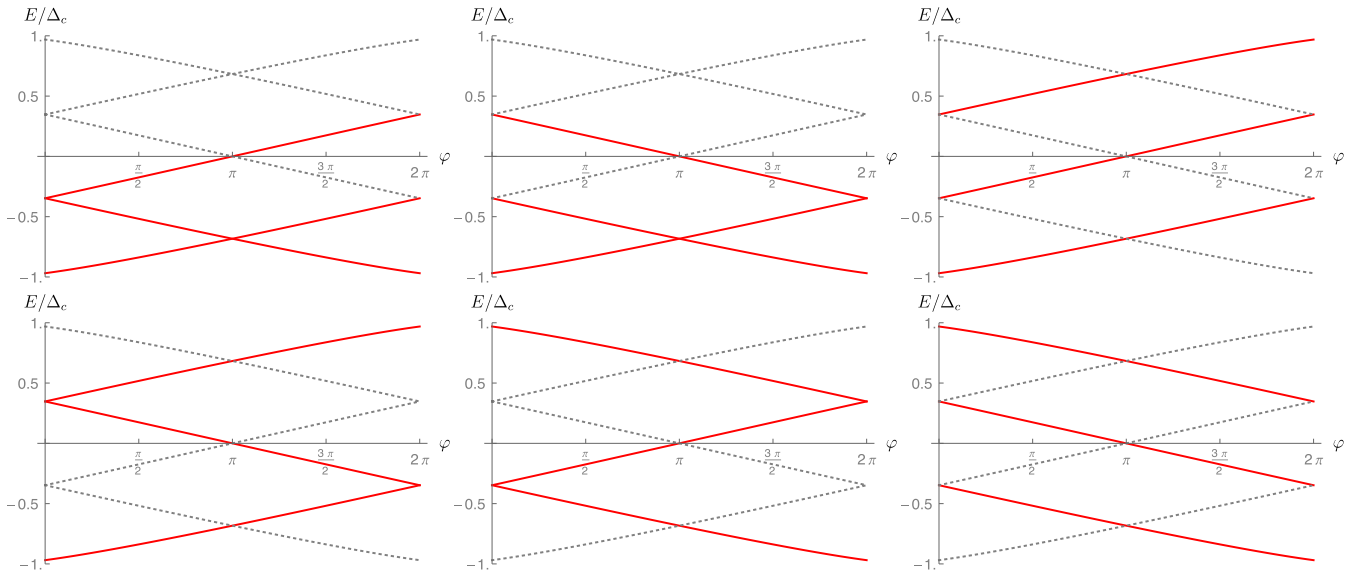

FIG. 10. Pictorial representation of the noninteracting many-body states in Eq. (A1). The first row displays states $|0;\varphi\rangle$, $|1;\varphi\rangle$, $|2;\varphi\rangle$ and second row displays states $|3;\varphi\rangle$, $|4;\varphi\rangle$, $|5;\varphi\rangle$, from left to right in both cases. The dashed gray lines (red full lines) correspond to empty (occupied) single-particle Andreev bound states. Scattering states are not shown.

The excitations can then be constructed as

$$
\begin{aligned}
|0;\varphi\rangle &= \left[\prod_{n>0} a_{n,+}\right]\left[\prod_{n>0} a_{n,-}\right][a_{0,+}]|\Omega_e\rangle,\\
|1;\varphi\rangle &= a^\dagger_{0,+}|0;\varphi\rangle,\\
|2;\varphi\rangle &= a^\dagger_{1,-}|0;\varphi\rangle,\\
|3;\varphi\rangle &= a^\dagger_{1,-}a^\dagger_{0,+}|0;\varphi\rangle,\\
|4;\varphi\rangle &= a^\dagger_{1,+}|0;\varphi\rangle,\\
|5;\varphi\rangle &= a^\dagger_{1,+}a^\dagger_{0,+}|0;\varphi\rangle.
\end{aligned}
\tag{A3}
$$

Enforcing the Nambu constraint, the normal ordered Hamiltonian for the junction reads as

$$
\begin{aligned}
:H_{\rm JJ}(\varphi): = {}& E_{0,+}(\varphi)a^\dagger_{0,+}a_{0,+} + \sum_{n>0,\tau} E_{n,\tau}(\varphi)a^\dagger_{n,\tau}a_{n,\tau}\\
&- \frac{1}{2}\left[E_{0,+}(\varphi) + \sum_{n>0,\tau} E_{n,\tau}(\varphi)\right]\\
&+ \frac{1}{2}\left[E_{0,+}(0) + \sum_{n>0,\tau} E_{n,\tau}(0)\right],
\end{aligned}
\tag{A4}
$$

which means that one first has to choose a reference state (here $|0;\varphi=0\rangle$), normal order with respect to it, and then consider the evolution of the phase φ to other values.

Figure 11 compares the results from the lattice and continuum models for the low-energy many-body spectrum. For each value of φ, we plot the excitation energies with respect to the ground state. For the continuum model, this is equivalent to normal ordering at each value of φ separately. This has the merit of canceling out the contribution from the scattering states. Consequently, the agreement between the lattice and continuum models is better than in Fig. 3. It is also worth

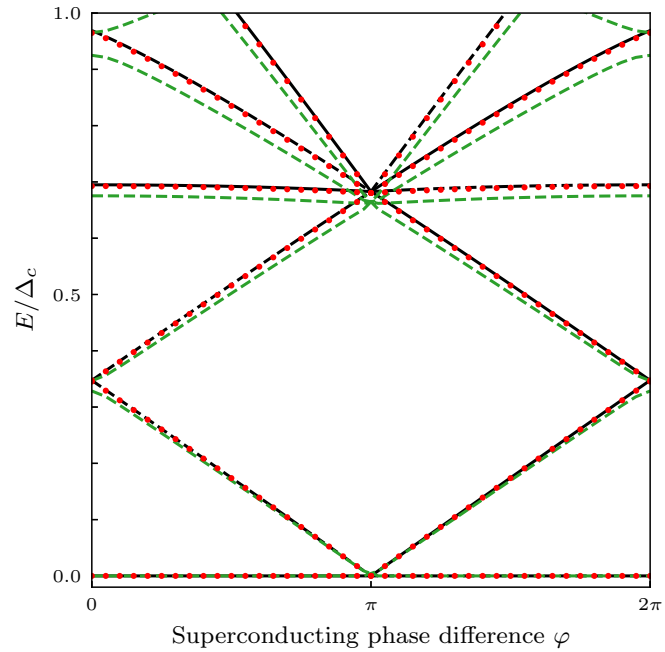

FIG. 11. Comparison between the analytical and exact diagonalization results for the noninteracting many-body spectrum. Only energy differences with respect to the lowest-energy states are considered at each φ. Black solid lines come from the continuum theory, red dots from the single-body lattice diagonalization, and green dashes from the many-body exact diagonalization; parameters are the same as used in the main text. The absence of the contributions from the continuum of scattering states leads to a better matching between both approaches, in comparison with Fig. 3. Splittings at $\varphi = 0, \pi$ due to $\mathcal{T}_-$-breaking terms are reduced for the single-particle calculation by considering scaled parameters such that ξ_0/a is scaled by a factor of 3.

noting that Fig. 11 corresponds to the energy peaks in the tunneling density of states of the junction [4], up to a selection rule that bars transitions to excited states with the same total fermion parity as the ground state.

APPENDIX B: CAVITY RENORMALIZATION AND INPUT-OUTPUT CALCULATION

In this Appendix, we show the derivation leading to Eqs. (33) and (36). The starting point is the Hamiltonian

$$H = H_S(\varphi) + H_{\rm cav} + H_I, \tag{B1}$$

where H_S is the JJ Hamiltonian with many-body eigenstates $|j;\varphi\rangle$ and many-body eigenvalues $E_j(\varphi)$,

$$H_{\rm cav} = \omega_0 a^\dagger a \tag{B2}$$

is the cavity Hamiltonian, and

$$H_I = g\hat{N}(a + a^\dagger) \tag{B3}$$

is the junction-cavity interaction.

The equation of motion for the cavity field reads as

$$\dot{\tilde{a}}(t) = -i[\tilde{a}(t), H] = -i(\omega_0\tilde{a}(t) + g\tilde{N}(t)), \tag{B4}$$

where tildes denote operators in the Heisenberg representation $[\tilde{a}(t) = e^{iHt}ae^{-iHt}$ and $\tilde{N}(t) = e^{iHt}\hat{N}e^{-iHt}]$. It is convenient to introduce the interaction picture via

$$\tilde{N}(t) = U^\dagger(t)N^i(t)U(t), \tag{B5}$$

where

$$U(t) = \exp\left[-i\int_{-\infty}^{t} dt' H_I^i(t')\right]. \tag{B6}$$

Assuming weak interactions, we expand

$$\tilde{N}(t) \approx N^i(t) + i\int_{-\infty}^{t} dt'\big[H_I^i(t'), N^i(t)\big]. \tag{B7}$$

Consequently, Eq. (B4) becomes

$$\begin{aligned}\dot{\tilde{a}}(t) &\approx -i\left(\omega_0\tilde{a}(t) + gN^i(t) + gi\int_{-\infty}^{t} dt'\big[H_I^i(t'), N^i(t)\big]\right)\\ &= -i\omega_0\tilde{a}(t) - igN^i(t)\\ &\quad + g^2\int_{-\infty}^{t} dt'(a^i(t') + a^{i\dagger}(t'))[N^i(t'), N^i(t)]\\ &\approx -i\omega_0\tilde{a}(t) - igN^i(t)\\ &\quad + g^2\int_{-\infty}^{t} dt'(\tilde{a}(t') + \tilde{a}^\dagger(t'))[N^i(t'), N^i(t)],\end{aligned} \tag{B8}$$

where we neglected higher-order terms in g in the last line.

Next, we write $\tilde{a}(t) = \tilde{a}_s(t)e^{-i\omega_0 t}$, where $\tilde{a}_s(t)$ evolves slowly in time. Also, to lowest order in g, we replace $[N^i(t'), N^i(t)]$ by its ground-state average. Then, Eq. (B8) can be approximated as

$$\dot{\tilde{a}}_s(t) \approx -igN^i(t)e^{i\omega_0 t} - g^2[C_-(t,\varphi)\tilde{a}_s(t) + C_+(t,\varphi)\tilde{a}_s^\dagger(t)], \tag{B9}$$

where

$$C_\pm(t,\varphi) = \int_{-\infty}^{t} dt' e^{i\omega_0(t\pm t')}\langle 0;\varphi|[N^i(t), N^i(t')]|0;\varphi\rangle. \tag{B10}$$

The correlation functions $C_\pm$ can be computed explicitly. First, we consider

$$\begin{aligned}C_-(t,\varphi) = \int_0^\infty d\tau \int \frac{d\omega_1 d\omega_2}{(2\pi)^2} e^{i(\omega_0-\omega_2)\tau} e^{i(\omega_1+\omega_2)t}\\ \times\langle 0,\varphi|[N^i(\omega_1), N^i(\omega_2)]|0,\varphi\rangle.\end{aligned} \tag{B11}$$

As usual, one writes

$$\begin{aligned}\int_0^\infty d\tau\, e^{i(\omega_0-\omega_2)\tau} &= \lim_{\epsilon\to 0}\int_0^\infty d\tau\, e^{i(\omega_0-\omega_2+i\epsilon)\tau}\\ &= P\frac{i}{(\omega_0-\omega_2)} + \pi\delta(\omega_0-\omega_2).\end{aligned} \tag{B12}$$

Therefore,

$$\begin{aligned}C_-(t,\varphi) = iP\int \frac{d\omega_1 d\omega_2}{(2\pi)^2}\frac{e^{i(\omega_1+\omega_2)t}}{\omega_0-\omega_2}\\ \times\langle 0;\varphi|[N^i(\omega_1), N^i(\omega_2)]|0;\varphi\rangle\\ + \frac{1}{2}\int\frac{d\omega_1}{2\pi}e^{i(\omega_1+\omega_0)t}\langle 0;\varphi|\\ \times[N^i(\omega_1), N^i(\omega_0)]|0;\varphi\rangle.\end{aligned} \tag{B13}$$

Using $\sum_j |j;\varphi\rangle\langle j;\varphi| = \mathbf{1}$ and recognizing that

$$\begin{aligned}\langle 0;\varphi|N^i(t)|j;\varphi\rangle &= e^{-i[E_0(\varphi)-E_j(\varphi)]t}\langle 0;\varphi|\hat{N}|j;\varphi\rangle\\ &\equiv e^{-i\Delta E_{0j}t}N_{0j},\end{aligned} \tag{B14}$$

we obtain

$$\begin{aligned}&\langle 0,\varphi|[N^i(t), N^i(t')]|0,\varphi\rangle\\ &\quad = -2i\sum_j \sin[\Delta E_{0j}(\varphi)(t-t')]|N_{0j}(\varphi)|^2.\end{aligned} \tag{B15}$$

Fourier transforming to frequency space, this gives

$$\begin{aligned}&\langle 0,\varphi|[N^i(\omega_1), N^i(\omega_2)]|0,\varphi\rangle\\ &\quad = (2\pi)^2\delta(\omega_1+\omega_2)\sum_j |N_{0j}(\varphi)|^2\\ &\qquad\times[\delta(\Delta E_{0j}(\varphi)-\omega_1) - \delta(\Delta E_{0j}(\varphi)+\omega_1)].\end{aligned} \tag{B16}$$

Substituting Eq. (B16) in Eq. (B13), we get

$$\begin{aligned}C_-(t,\varphi) = -2i\sum_j |N_{0j}(\varphi)|^2\frac{\Delta E_{0j}(\varphi)}{\omega_0^2 - (\Delta E_{0j}(\varphi))^2}\\ + \pi\sum_j |N_{0j}(\varphi)|^2[\delta(\Delta E_{0j}(\varphi)+\omega_0) - (\omega_0\to-\omega_0)].\end{aligned} \tag{B17}$$

Proceeding similarly for C_+, we find

$$C_+(t,\varphi) = -2ie^{i2\omega_0 t}\sum_j |N_{0j}(\varphi)|^2 \frac{\Delta E_{0j}(\varphi)}{\omega^2 - (\Delta E_{0j}(\varphi))^2} + \pi e^{i2\omega_0 t}\sum_j |N_{0j}(\varphi)|^2 \times [\delta(\Delta E_{0j}(\varphi) - \omega_0) - \delta(\Delta E_{0j}(\varphi) + \omega_0)]. \tag{B18}$$

The fact that $C_+(t)$ varies rapidly in time ($\propto e^{2i\omega_0 t}$) means that it can be discarded in the rotating wave approximation. We finally obtain, back in the original time frame,

$$\dot{\tilde{a}}(t) \approx -i\omega_0\tilde{a}(t) - igN^i(t) - g^2 C_-(t,\varphi)\tilde{a}(t). \tag{B19}$$

The imaginary part of C_- renormalizes the cavity resonance frequency $\omega_0 \to \omega_0 + \bar{\omega}$, where

$$\bar{\omega} = 2g^2\sum_j |N_{0j}(\varphi)|^2 \frac{\Delta E_{0j}(\varphi)}{(\Delta E_{0j}(\varphi))^2 - \omega_0^2}. \tag{B20}$$

The real part of C_+ describes the junction-induced decay of cavity photons, with rate

$$\bar{\kappa} \equiv 2\pi g^2 \sum_j |N_{0j}(\varphi)|^2 \times [\delta(\Delta E_{0j}(\varphi) + \omega_0) - \delta(\Delta E_{0j}(\varphi) - \omega_0)]. \tag{B21}$$

Therefore,

$$\dot{\tilde{a}}(t) \approx -\left(i(\omega_0 + \bar{\omega}) + \frac{\bar{\kappa}}{2}\right)\tilde{a}(t) - igN^i(t). \tag{B22}$$

In the presence of input fields, their coupling with the cavity induces an additional damping κ_0 for the cavity photons [29], so that

$$\dot{\tilde{a}}(t) = -\left(i\omega_R + \frac{\kappa_R}{2}\right)\tilde{a}(t) - igN^i(t) + \sqrt{\kappa_0}\tilde{b}_{\rm in}(t), \tag{B23}$$

where $\omega_R = \omega_0 + \bar{\omega}$ and $\kappa_R = \kappa_0 + \bar{\kappa}$. This completes the derivation of Eq. (33) of the main text.

From Eq. (B23), one can readily derive Eq. (36) of the main text. First, recall that the output field can be related to the input field by the boundary condition

$$\tilde{b}_{\rm out}(t) = \sqrt{\kappa_0}\tilde{a}(t) - \tilde{b}_{\rm in}(t). \tag{B24}$$

Combining the Fourier transforms of Eqs. (B24) and (B23), we obtain

$$\tilde{b}_{\rm out}(\omega) = \frac{-\left[\omega - \omega_R - i\frac{\kappa_0 - \bar{\kappa}}{2}\right]\tilde{b}_{\rm in}(\omega) + g\sqrt{\kappa_0}N^i(\omega)}{\omega - \omega_R + i\kappa_R/2}. \tag{B25}$$

Noting that $\langle 0;\varphi|N^i(\omega)|0;\varphi\rangle \propto \delta(\omega)$, and recalling that we are interested in the response at frequencies close to ω_0, we write

$$\langle\tilde{b}_{\rm out}(\omega)\rangle = \frac{-\left[\omega - \omega_R - i\frac{\kappa_0 - \bar{\kappa}}{2}\right]\langle\tilde{b}_{\rm in}(\omega)\rangle}{\omega - \omega_R + i\kappa_R/2}. \tag{B26}$$

From here, the expressions for the reflection coefficient and phase shift quoted in the main text can be recovered.

[1] D. Averin and A. Bardas, Phys. Rev. Lett. **75**, 1831 (1995).
[2] H.-Y. Hui and J. D. Sau, Phys. Rev. B **95**, 014505 (2017).
[3] L. Fu and C. L. Kane, Phys. Rev. B **79**, 161408 (2009).
[4] F. Zhang and C. L. Kane, Phys. Rev. Lett. **113**, 036401 (2014).
[5] C. P. Orth, R. P. Tiwari, T. Meng, and T. L. Schmidt, Phys. Rev. B **91**, 081406 (2015).
[6] R. S. Deacon, J. Wiedenmann, E. Bocquillon, F. Domínguez, T. M. Klapwijk, P. Leubner, C. Brüne, E. M. Hankiewicz, S. Tarucha, K. Ishibashi, H. Buhmann, and L. W. Molenkamp, Phys. Rev. X **7**, 021011 (2017).
[7] E. Bocquillon, R. S. Deacon, J. Wiedenmann, P. Leubner, T. M. Klapwijk, C. Brune, K. Ishibashi, H. Buhmann, and L. W. Molenkamp, Nat. Nanotechnol. **12**, 137 (2016).
[8] J. Wiedenmann, E. Bocquillon, R. S. Deacon, S. Hartinger, O. Herrmann, T. M. Klapwijk, L. Maier, C. Ames, C. Brüne, C. Gould, A. Oiwa, K. Ishibashi, S. Tarucha, H. Buhmann, and L. W. Molenkamp, Nat. Commun. **7**, 10303 (2016).
[9] F. Domínguez, O. Kashuba, E. Bocquillon, J. Wiedenmann, R. S. Deacon, T. M. Klapwijk, G. Platero, L. W. Molenkamp, B. Trauzettel, and E. M. Hankiewicz, Phys. Rev. B **95**, 195430 (2017).
[10] Y. Peng, Y. Vinkler-Aviv, P. W. Brouwer, L. I. Glazman, and F. von Oppen, Phys. Rev. Lett. **117**, 267001 (2016).
[11] D. Sticlet, J. D. Sau, and A. Akhmerov, Phys. Rev. B **98**, 125124 (2018).
[12] Y. Vinkler-Aviv, P. W. Brouwer, and F. von Oppen, Phys. Rev. B **96**, 195421 (2017).
[13] A. Y. Kitaev, Phys. Usp. **44**, 131 (2001).
[14] R. Aguado, Riv. Nuovo Cimento **40**, 523 (2017).
[15] C. J. Pedder, T. Meng, R. P. Tiwari, and T. L. Schmidt, Phys. Rev. B **96**, 165429 (2017).
[16] A. Blais, R.-S. Huang, A. Wallraff, S. M. Girvin, and R. J. Schoelkopf, Phys. Rev. A **69**, 062320 (2004).
[17] A. Cottet, T. Kontos, and B. Douçot, Phys. Rev. B **88**, 195415 (2013).
[18] O. Dmytruk, M. Trif, and P. Simon, Phys. Rev. B **92**, 245432 (2015).
[19] O. Dmytruk, M. Trif, and P. Simon, Phys. Rev. B **94**, 115423 (2016).
[20] M. Hays, G. de Lange, K. Serniak, D. J. van Woerkom, D. Bouman, P. Krogstrup, J. Nygård, A. Geresdi, and M. H. Devoret, Phys. Rev. Lett. **121**, 047001 (2018).
[21] C. Müller, J. Bourassa, and A. Blais, Phys. Rev. B **88**, 235401 (2013).
[22] M. C. Dartiailh, T. Kontos, B. Douçot, and A. Cottet, Phys. Rev. Lett. **118**, 126803 (2017).
[23] J. I. Väyrynen, G. Rastelli, W. Belzig, and L. I. Glazman, Phys. Rev. B **92**, 134508 (2015).
[24] P. L. e S. Lopes, J. C. Y. Teo, and S. Ryu, Phys. Rev. B **95**, 235134 (2017).
[25] D. B. Kaplan, Lectures on effective field theory-ICTP-SAIFR (2016) (unpublished).

[26] C. W. J. Beenakker and H. van Houten, in *Nanostructures and Mesoscopic Systems*, edited by W. P. Kirk and M. A. Reed (Academic Press, 1992), pp. 481–497.

[27] S. Ryu, A. P. Schnyder, A. Furusaki, and A. W. W. Ludwig, New J. Phys. **12**, 065010 (2010).

[28] T. Giamarchi, *Quantum Physics in One Dimension* (Oxford University Press, Oxford, 2004).

[29] D. F. Walls and G. F. Milburn, *Quantum Optics* (Springer, Berlin, 2008).

[30] S. J. Bosman, M. F. Gely, V. Singh, A. Bruno, D. Bothner, and G. A. Steele, npj Quantum Inf. **3**, 46 (2017).

[31] T. Walter, P. Kurpiers, S. Gasparinetti, P. Magnard, A. Potočnik, Y. Salathé, M. Pechal, M. Mondal, M. Oppliger, C. Eichler, and A. Wallraff, Phys. Rev. Appl. **7**, 054020 (2017).

[32] H. Zhang, C.-X. Liu, S. Gazibegovic, D. Xu, J. A. Logan, G. Wang, N. van Loo, J. D. S. Bommer, M. W. A. de Moor, D. Car, R. L. M. Op het Veld, P. J. van Veldhoven, S. Koelling, M. A. Verheijen, M. Pendharkar, D. J. Pennachio, B. Shojaei, J. S. Lee, C. J. Palmstrøm, E. P. A. M. Bakkers *et al.*, Nature (London) **556**, 74 (2018).

[33] W. Chang, S. M. Albrecht, T. S. Jespersen, F. Kuemmeth, P. Krogstrup, J. Nygård, and C. M. Marcus, Nat. Nanotechnol. **10**, 232 (2015).

[34] R. M. Lutchyn, E. P. A. M. Bakkers, L. P. Kouwenhoven, P. Krogstrup, C. M. Marcus, and Y. Oreg, Nat. Rev. Mater. **3**, 52 (2018).

[35] W. De Gottardi, D. Sen, and S. Vishveshwara, New J. Phys. **13**, 065028 (2011).